Hierarchical nickel sulfide/carbon nanotube nanocomposite as a catalytic material toward triiodine reduction in dye-sensitized solar cells

Man-Ning Lu [a], Chao-Shuan Dai [b], Sheng-Yen Tai [a], Tsung-Wu Lin [b, *], Jeng-Yu Lin [a, *]
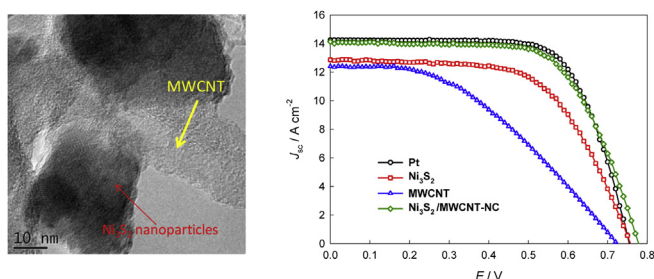
[a] Dept. of Chemical Engineering, Tatung University, No. 40, Sec. 3, Chungshan North Rd., Taipei City 104, Taiwan
[b] Dept. of Chemistry, Tunghai University, No. 181, Sec. 3, Taichung Port Rd., Taichung City 40704, Taiwan

HIGHLIGHTS

- Ni_3S_2/MWCNT-NC was synthesized via a facile glucose-assisted hydrothermal method.
- Annealed Ni_3S_2/MWCNT-NC CE showed improved catalytic activity for I_3^- reduction.
- Ni_3S_2 and conductive MWCNTs imparted high catalytic activity and stability to the catalyst.
- The DSC with the annealed Ni_3S_2/MWCNT-NC CE reached an efficiency of 6.87%.
- Ni_3S_2/MWCNT-NC CE served as an inexpensive and promising alternative to Pt CE for DSCs.

GRAPHICAL ABSTRACT

ABSTRACT

In this study, Ni_3S_2 nanoparticles are successfully decorated on the backbone of conductive multi-walled carbon nanotubes (denoted as Ni_3S_2/MWCNT-NC) via a facile glucose-assisted hydrothermal method and employed as a counter electrode (CE) in dye-sensitized solar cells (DSCs). It is noteworthy that the use of glucose in the hydrothermal reaction plays a crucial role in the formation of the nanocomposite structure. Nevertheless, a thick layer of amorphous carbon derived from the hydrothermal carbonization of glucose covers Ni_3S_2 nanoparticle surface, and thus may inhibit the contact of active sites in Ni_3S_2 nanoparticles with electrolyte. It is found that the partial amorphous carbon on Ni_3S_2/MWCNT-NC can be effectively removed after annealing at 400 °C in a nitrogen atmosphere, which further increases the active sites of Ni_3S_2 nanoparticles on MWCNTs and therefore improves the electrocatalytic activity of the Ni_3S_2/MWCNT-NC CE. As a result, the DSC with the Ni_3S_2/MWCNT-NC CE yields a cell efficiency of 6.87%, which is higher than those of DSCs based on the Ni_3S_2 CE (5.77%) and MWCNT CE (3.76%). Because the Ni_3S_2/MWCNT-NC CE based DSC shows a comparable photovoltaic performance to the DSC using the Pt CE (7.24%), Ni_3S_2/MWCNT-NC CE may serve as a promising alternative to Pt CE for DSCs.

© 2014 Elsevier B.V. All rights reserved.

1. Introduction

Since dye-sensitized solar cell (DSC) was reported by Grätzel and co-workers in 1991, it has become one of most promising photovoltaic devices due to its inherent virtues of simple

* Corresponding authors. Fax: +886 225861939.
E-mail addresses: twlin@thu.edu.tw (T.-W. Lin), jylin@ttu.edu.tw, d923615@gmail.com (J.-Y. Lin).

preparation, low cost and relatively high photovoltaic cell efficiency (PCE) [1,2]. Typically, a DSC comprises a dye-sensitized TiO_2 nanocrystalline film as a photoanode, a counter electrode (CE), and an electrolyte traditionally containing a triiodide/iodide (I_3^-/I^-) redox couple. As one of the crucial and indispensable component in DSCs, CEs serve to collect electrons from external circuit and accelerate the I_3^- reduction reaction. Therefore, a CE with the characteristics of both excellent electrocatalytic activity and high electrical conductivity is desirable [3]. Up to now, noble Pt metal with high conductivity and electrocatalytic activity has been widely used as a CE material. Nevertheless, Pt is very expensive and easily corroded by I_3^-/I^- based redox electrolyte, thus possibly resulting in the restriction for large-scale production of DSCs in the future. Nowadays, a great deal of efforts have been made to explore Pt-like alternatives such as carbonaceous materials [4–12], conducting polymers, [13] transition metal oxides [14], nitrides [15], carbide [16,17], and sulfides [18–22].

Carbonaceous materials including carbon black, [4] graphite, [5] activated carbon, [6,7] carbon nanotubes (CNTs) [8–10], and graphene [11,12] have also been regarded as the potential alternatives for Pt due to their features of low cost, reasonable electron-transport ability, and high corrosion resistance. Among them, multi-walled carbon nanotubes (MWCNTs) have attracted much attention due to their exceptional specific surface area, high electrical conductivity, excellent mechanical strength and good thermal/chemical stability [23]. However, their intrinsically electrocatalytic activity for I_3^- reduction is not satisfactory owing to the limited number of active sites for I_3^- reduction on MWCNT surface. [24] To further increase the active sites for I_3^- reduction and improve the PCE of CNT-based DSCs, extensive studies have been recently focused on decorating the surface of CNTs with intrinsically electrocatalytic nanoparticles such as metal oxides, nitrides and sulfide [25–27]. For example, Zhang et al. [28] reported that the synthesis of the transparent conducting oxide (TCO)-free and Pt-free CE involves that the single-walled CNTs (SWCNTs) were spray-coated onto a glass substrate to form a thin film and then NiS precursor dispersed onto the resulting SWCNT film was annealed in argon to obtain the composite CE. Nevertheless, the DSC based on Ni_3S_2/SWCNT composite CE only provided a conversion efficiency of 2.76%. Very recently, Xiao et al. [29] prepared NiS/MWCNT composite CE by electrophoretic deposition of MWCNTs on Ti substrate and followed by the electrodeposition of NiS onto MWCNTs. The DSC assembled with the NiS/MWCNT/Ti CE achieved an impressive cell efficiency of 7.90%. However, the aforementioned nickel sulfide/CNT composites were prepared via two-step method which possibly results in that nickel sulfide is only deposited on the top surface of CNT layer or the inhomogeneous coating of nickel sulfides on the whole conductive CNT network.

In this study, we develop a facile one-pot hydrothermal method to directly grow the Ni_3S_2 nanoparticles on MWCNT backbones. In this hydrothermal synthesis, the addition of glucose can serve as the binder to allow the homogeneous dispersion of Ni_3S_2 nanoparticles on the MWCNT surface. We used this hierarchical Ni_3S_2/MWCNT nanocomposite (denoted as Ni_3S_2/MWCNT-NC) as the CE material in DSCs and characterized its electrocatalytic activity towards the reduction of I_3^- to I^-. Due to the synergetic effect of Ni_3S_2 and MWCNTs, the DSC assembled with Ni_3S_2/MWCNT-NC CE shows the improved photovoltaic performance and excellent long-term stability.

2. Experimental section

2.1. Synthesis of Ni_3S_2/MWCNT-NC

The multi-walled CNTs were purchased from Thomas Swan & Co. Ltd. The diameters of CVD synthesized MWCNTs range from 10 to 20 nm and their wall thicknesses range from 3 to 6 nm. The purchased MWCNT product consisted of low inorganic residue (5 wt %) and 70 wt % nanotube contents. The purification of MWCNTs was achieved by refluxing MWCNTs (0.5 g) in concentrated nitric acid (100 mL) at 120 °C for 12 h. After the reaction, the MWCNT precipitate was filtered off, washed with distilled water, and dried in air. For the synthesis of Ni_3S_2/MWCNT-NC, acid-treated MWCNTs (7.5 mg) and glucose (90 mg) were added to the mixture solution of ethanol (9 mL) and distilled water (1 mL). The mixed solution was sonicated for 20 min to make a homogeneous dispersion and then nickel chloride (195 mg), thiourea (76 mg), and 1 mL of ammonia were added to the MWCNT dispersion. The mixture was then transferred to a stainless-steel autoclave (20 mL capacity). After sealing, the autoclave was heated to 180 °C for 12 h and then cooled to room temperature. Finally, the precipitate was filtered off, washed with distilled water, and dried in air. In a separate experiment, the Ni_3S_2 powder was also synthesized using the glucose-assisted hydrothermal method. Except for the addition of MWCNTs, the synthetic procedures for Ni_3S_2 powder are the same as those for Ni_3S_2/MWCNT-NC. For the synthesis of the mixture of Ni_3S_2 and MWCNTs, the synthetic procedures for Ni_3S_2/MWCNT-NC were followed except for the addition of glucose in the hydrothermal reaction. As shown in Fig. S1, Ni_3S_2 particles are separated from MWCNTs and there is no coating of amorphous carbon on the mixture when glucose is absent in the hydrothermal synthesis.

2.2. Fabrication of DSCs

The TiO_2 films (0.16 cm^2) with a bilayer structure composed of a dense layer (~12 μm, ETERDSC Ti 2105, Eternal Chemical CO.) and a scattering layer (~2 μm, ETERDSC Ti 2325, Eternal Chemical CO.) were fabricated on the ultrasonically cleaned FTO glass substrates (7 Ω sq^{-1}, NSG) by using the screen-printing technique. The TiO_2 films were sintered at 450 °C for 30 min, and then subsequently cooled to 80 °C. Then, the sintered TiO_2 films were immersed in the 0.3 mM N719 dye (Everlight Chemical Industry Co.) for 12 h at a room temperature. The dye-sensitized TiO_2 photoanodes were assembled with CEs into sandwich-type configuration and sealed with hot-melt Surlyns (DuPont, 30 μm). After that, the redox electrolyte containing 1 M 1,3-dimethylimidazolium iodide (Merck), 0.5 M 4-tert-butylpyridine (Aldrich), 0.15 M iodine (J.T. Baker), and 0.1 M guanidine thiocyanate (Aldrich) in 3-methoxypropionitrile (Acros) was injected into the sandwich-type cells via the predrilled holes on the CEs.

To prepare CEs, the active materials including Ni_3S_2, MWCNTs, and Ni_3S_2/MWCNT-NC, were mixed with acetylene black and polyvinyldifluoride in a weight ratio of 8:1:1. The aforementioned mixture was added to N-methyl-2-pyrrolidone and the resulting slurry was grounded for 2 h. Then, the obtained slurry was coated onto the drilled FTO glass substrates by the doctor-blading technique to form the films with a thickness ca. of 4 μm. Finally, the coated FTO glass was sintered in a N_2 atmosphere at 400 °C for 1 h. For comparison, 100 nm thick Pt film was sputtered onto a FTO lass substrate as a CE by a DC sputtering instrument (ULVAC).

2.3. Material characterizations

A field-emission transmission electron microscope (TEM, JEOL JEM-2100F, operated at 200 kV with a point-to-point resolution of 0.19 nm) equipped with an energy dispersive spectrometer (EDS) was used to obtain the information on the microstructures and the chemical compositions. The X-ray powder diffraction (XRD) pattern of the composite was obtained from Philips X'Pert Pro MPD. All thermogravimetric analysis (TGA) experiments were performed

using a Pyris 1 TGA (Perkin Elmer) with N_2 as a purge gas at a flow rate of 100 sccm. The samples were heated from room temperature to 400 °C at a heating rate of 5 °C min^{-1}, and then held at that temperature for 1 h. The Brunauer—Emmett—Teller (BET) specific surface area was analyzed using a CBET-201A (Porous Materials, Inc.) analyzer by nitrogen absorption. The following electrochemical measurements were carried out using a CHI614d potentiostat. The cyclic voltammetry (CV) was performed in 3-methoxypropionitrile solution consisting of 50 mM LiI, 10 mM I_2, and 50 mM LiClO$_4$ using a three-electrode system, in which the as-prepared CE, a Pt sheet and a Pt wire served as the working, counter and reference electrodes, respectively. The electrochemical impedance spectroscopy (EIS) measurements were conducted using the symmetric configuration cells composed of two identical CEs. EIS measurements were performed at the zero bias voltage using a potentiostat (IM6, Zahner) equipped with a frequency analyzer (Thales). An AC voltage with 5 mV amplitude in a frequency range of 0.1 Hz—50 kHz was applied The Nyquist plots were fitted by the software ZSimpWin version 3.1. The photovoltaic characteristics of DSCs were analyzed under the light exposure (100 mW cm^{-2}, Yamashita Denso YSS-150A, AM 1.5G) which was calibrated with a radiant power/energy meter (Oriel, 70260).

3. Results and discussion

Fig. 1a shows the typical TEM image of Ni$_3$S$_2$/MWCNT-NC. It is clear to see that conductive MWCNTs can serve as the backbone where the Ni$_3$S$_2$ nanoparticles with the diameters ranging from 10 to 80 nm are deposited. The high surface area of MWCNTs allows a number of Ni$_3$S$_2$ nanoparticles to be homogeneously deposited onto the MWCNT surface. When MWCNTs are absent in the hydrothermal synthesis, the diameters of the as-synthesized Ni$_3$S$_2$ particles range from 0.5 to 4 μm (Fig. S2). This drastic size difference highlights the important role of MWCNTs as an effective substrate for the growth of nanomaterials. The previous studies of the graphene or CNT based composites have verified that the carbon nanomaterials with high surface area can serve as a good substrate to avoid the aggregation of deposited materials [30,31], which is consistent with our finding. It is noteworthy that the use of glucose in the hydrothermal reaction plays a crucial role in the formation of the hierarchical structure. As shown in Fig. 1b a thick layer of amorphous carbon (1—3 nm) derived from the hydrothermal carbonization of glucose covers both MWCNT and Ni$_3$S$_2$ nanoparticle surface and thus serves as a binder to assist the growth of nanoparticles along the longitudinal axis of MWCNTs [32]. In contrast, the sample prepared without glucose is a mixture of MWCNTs and Ni$_3$S$_2$ particles, in which the MWCNTs just act as

wires that connect Ni$_3$S$_2$ particles (Fig. S1). Based on these observations, it is clear that glucose plays a crucial role in the formation of the Ni$_3$S$_2$/MWCNT-NC. The previous study of the growth of MoS$_2$ nanosheets on the CNT backbone has suggested that glucose might mediate the formation of MoS$_2$ nanosheets with smaller size and it could meanwhile serve as a binder to help the MoS$_2$ nanosheets to grow on the surface of CNTs with uniform coverage along the longitudinal axis [33]. Furthermore, our previous study has proved that the irregularly shaped Ni$_3$S$_2$ particles on MWCNTs are actually consisted of nanoparticles with the smaller size [32]. In the hydrothermal reaction, the growth mechanism of Ni$_3$S$_2$ nanoparticles on MWCNTs may involve that the amorphous carbon produced by the hydrothermal carbonization of glucose is intercalated between the small-sized nanoparticles. In other words, the amorphous carbon serves as a binder for the assembly of Ni$_3$S$_2$ nanoparticles. Finally, the Ni$_3$S$_2$ particles with diameters of several tens of nanometers are attached onto the MWCNT surface via the assistance of carbonaceous glue. However, the presence of the amorphous carbon on Ni$_3$S$_2$ nanoparticles may act as a passive layer, which inhibits the contact of active sites in Ni$_3$S$_2$ nanoparticles with the electrolyte. Our previous study has demonstrated that the activity of Ni$_3$S$_2$/MWCNT-NC towards hydrogen evolution can be significantly enhanced when the layer of amorphous carbon on Ni$_3$S$_2$ nanoparticles is partly removed by base treatment [34]. On the other hand, the complete removal of amorphous carbon may damage the intimate contact between the Ni$_3$S$_2$ nanoparticles and the MWCNTs, which deteriorates the delivery of the electrons from MWCNTs to the Ni$_3$S$_2$ nanoparticles. In this study, it is found that the annealing Ni$_3$S$_2$/MWCNT-NC in a nitrogen atmosphere at 400 °C is an effective method to remove a part of amorphous carbon in Ni$_3$S$_2$/MWCNT-NC.

Fig. 2a shows the typical TGA curve for the mixture of Ni$_3$S$_2$ and MWCNTs. Due to no use of glucose in a hydrothermal reaction, the weight loss of the mixture of Ni$_3$S$_2$ and MWCNTs is ca. 14% after TGA experiment. In contrast, Ni$_3$S$_2$/MWCNT-NC shows much more weight loss (37%) than the mixture of Ni$_3$S$_2$ and MWCNTs due to the decomposition of amorphous carbon at the high temperature. To further characterize the composition of the annealed composite, XRD measurement was carried out. As shown Fig. 2b, all the identified peaks except the (002) reflection of MWCNTs can be attributed to the Ni$_3$S$_2$ phase (JCPDS card No. 30-0863), suggesting that no oxide formation occurs during annealing process. Fig. 2c shows the typical TEM image of Ni$_3$S$_2$/MWCNT-NC after annealing treatment. It is observed that Ni$_3$S$_2$ nanoparticles are still firmly attached onto MWCNT surface and the density of Ni$_3$S$_2$ nanoparticles on MWCNTs seems to remain unchanged. Furthermore, the extensive high resolution TEM analyses (Fig. 2d) reveal that the
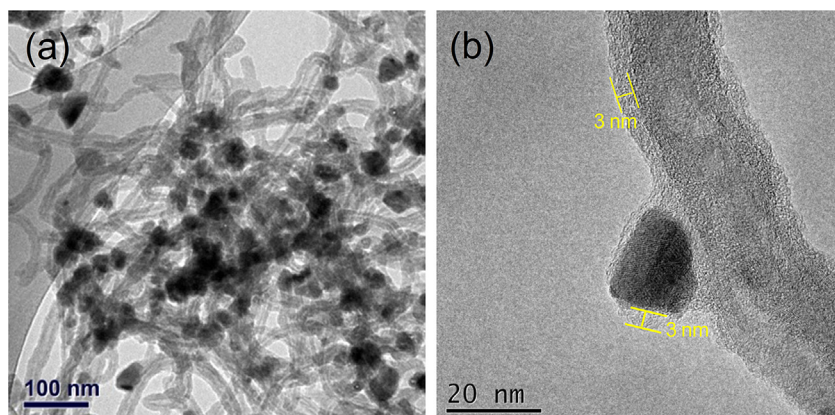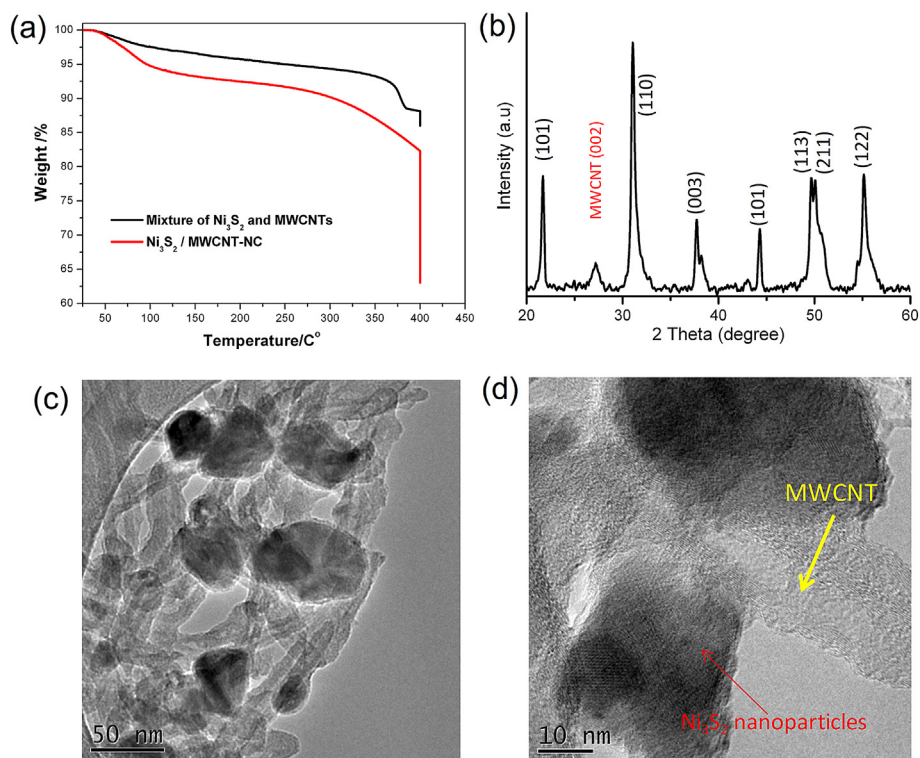

**Fig. 1.** (a) TEM and (b) high resolution TEM images of Ni$_3$S$_2$/MWCNT-NC.

Fig. 2. (a) TGA curves of Ni$_3$S$_2$/MWCNT-NC and the mixture of Ni$_3$S$_2$ and MWCNTs. (b) XRD pattern, (c) TEM, and (d) High resolution TEM images of the annealed Ni$_3$S$_2$/MWCNT-NC.

amorphous carbon on MWCNTs and Ni$_3$S$_2$ nanoparticles are partly removed after annealing treatment, which increases the exposure of the active sites in Ni$_3$S$_2$ nanoparticles. As shown in Fig. S3, the EDS analysis of the annealed Ni$_3$S$_2$/MWCNT-NC displays the presence of C, Ni and S elements and the atomic ratio of Ni to S is estimated to be 3.0:2.0.

To compare the electrocatalytic activities of as-prepared and annealed Ni$_3$S$_2$/MWCNT-NC CEs, CV measurements were conducted under the same conditions. As shown in Fig. 3a, two typical pairs of oxidation and reduction peaks can be clearly observed for the annealed Ni$_3$S$_2$/MWCNT-NC CE. The resultant positive pair is assigned to the redox reaction of I$_2$/I$_3^-$ (3I$_2$ + 2e$^-$ ↔ 2I$_3^-$) and the negative pair is ascribed to the redox reaction of I$_3^-$/I$^-$ (I$_3^-$ + 2e$^-$ ↔ 3I$^-$). In contrast, no redox peaks is observed for the as-prepared Ni$_3$S$_2$/MWCNT-NC CE. This result suggests that the partial removal of the amorphous carbon formed on Ni$_3$S$_2$/MWCNT-NC

leads to increasing the exposure of the active sites in Ni$_3$S$_2$ nanoparticles, which enhances the electrocatalytic activity of Ni$_3$S$_2$/MWCNT-NC CE. The electrocatalytic activity of annealed Ni$_3$S$_2$/MWCNT-NC CE is further compared with those of pristine Ni$_3$S$_2$, MWCNT, and Pt CEs. As shown in Fig. 3b, two pairs of redox peaks are observed for all CEs. Since the function of CE is mainly responsible for catalyzing the reduction of I$_3^-$ to I$^-$ in a typical DSC, the characteristics of the negative redox pair are at the focus of our investigation. It is noteworthy that the annealed Ni$_3$S$_2$/MWCNT-NC CE shows the higher redox peak current densities than the pristine Ni$_3$S$_2$, MWCNT and Pt CEs. To investigate the origin for the relatively high current densities of the annealed Ni$_3$S$_2$/MWCNT-NC CE, BET specific surface area (σ) for pristine Ni$_3$S$_2$, MWCNT, and Ni$_3$S$_2$/MWCNT-NC powders were measured and summarized in Table 1. It can be found that Ni$_3$S$_2$/MWCNT-NC possesses the larger BET specific surface area of 137.6 m^2 g^{-1} than those of pristine Ni$_3$S$_2$
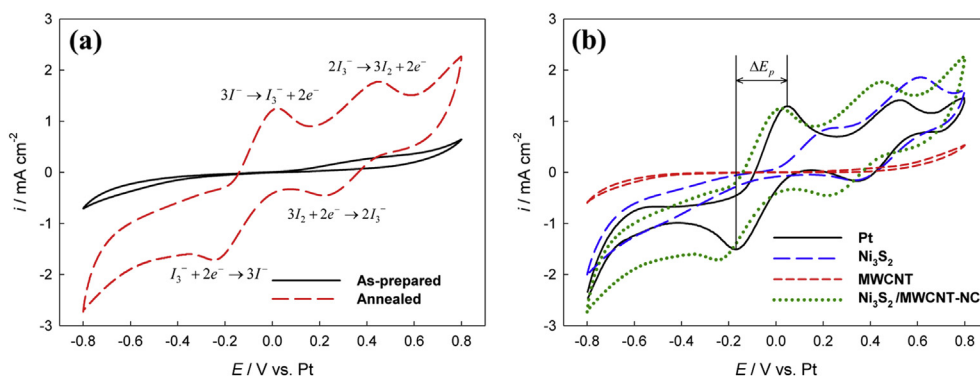
Fig. 3. (a) CV curves of I$_2$/I$_3^-$ system for the as-prepared and annealed Ni$_3$S$_2$/MWCNT-NC CEs. (b) CV curves of I$_2$/I$_3^-$ system for the Pt, Ni$_3$S$_2$, MWCNT, and the annealed Ni$_3$S$_2$/MWCNT-NC CEs.

Table 1
BET specific surface area and electrochemical parameters for the Pt, Ni_3S_2, MWCNT, and Ni_3S_2/MWCNT-NC CEs.

	σ/m^2 g^{-1}	ΔE_p/mV	R_s/Ω	R_{ct}/Ω	Z_N/Ω	J_0/mA cm^{-2}
Pt	–	224	9.14	6.82	2.48	3.11
Ni_3S_2	32.3	729	12.78	15.21	50.61	0.83
MWCNT	105.8	746	10.15	22.82	21.37	0.25
Ni_3S_2/MWCNT-NC	137.6	252	10.76	9.11	26.73	2.66

(32.3 m^2 g^{-1}) and MWCNT (105.8 m^2 g^{-1}). Therefore, the enhancement in the current densities of Ni_3S_2/MWCNT-NC CE can be attributed to the fact that the Ni_3S_2 nanoparticles well-dispersed on the surface of MWCNT remarkably increase the number of catalytic sites for I_3^- reduction. Additionally, another factor to evaluate the electrocatalytic activity of a CE is the potential separation between oxidation and reduction peaks (ΔE_p), which is inversely associated with the electrochemical rate constant of a redox reaction [35,36]. The annealed Ni_3S_2/MWCNT-NC CE possesses a relatively lower ΔE_p (252 mV) than the pristine Ni_3S_2 CE (729 mV) and the MWCNT CE (746 mV), and this ΔE_p value is even comparable to that of the Pt CE (224 mV). Compared with the pristine Ni_3S_2 CE, the higher current densities and faster electrochemical rate of the annealed Ni_3S_2/MWCNT-NC CE can be attributed to its excellent intrinsic electrocatalytic activity and electrical conductivity. These results reveal the synergetic effects of the Ni_3S_2 and MWCNTs on catalyzing the I_3^- reduction reaction, which can efficiently reduce the polarization resistance and increase the active catalytic sites [37,38].

To further get the deep insights into the electrocatalytic activities of the pristine Ni_3S_2, MWCNT, Ni_3S_2/MWCNT-NC and Pt CEs, EIS and Tafel polarization measurements were performed with symmetrical configuration composed of two identical CEs (CE/redox electrolyte/CE). Fig. 4a presents the Nyquist plots of various symmetrical cells where the composition of the redox electrolyte is the same as that used in DSCs. Furthermore, the equivalent circuit used to simulate the Nyquist plots of various symmetrical cells is shown in Fig. S4. This equivalent circuit contains ohmic series resistance (R_s), charge-transfer resistance (R_{ct}), constant phase element (CPE) at the CE/electrolyte interface, and Nernst diffusion impedance (Z_N) of the I_3^-/I^- redox couple in the bulk electrolyte. The fitted results are listed in Table 1. In Fig. 4a, the intercept of the semicircle on the real axis is assigned to the R_s. The R_{ct}, a direct parameter to evaluate the electrocatalytic activity of a CE, can be estimated as half of the value of the real component of impedance at the high-frequency region semicircle, whereas the semicircle in low-frequency region represents the Z_N of the I_3^-/I^- redox couple in the electrolyte [39]. Due to the combination with highly conductive

MWCNTs, the Ni_3S_2/MWCNT-NC CE shows a lower R_s (10.76 Ω) compared to the pristine Ni_3S_2 (12.78 Ω). Additionally, it is noteworthy that the Ni_3S_2/MWCNT-NC CE shows a lower R_{ct} (9.11 Ω) than the pristine Ni_3S_2 (15.21 Ω) and MWCNT (22.82 Ω) CEs and this R_{ct} value is even comparable to that of Pt CE (6.82 Ω). This low R_{ct} can be attributed to the synergetic effects of the highly conductive MWCNT framework and the highly electrocatalytic Ni_3S_2 nanoparticles [25,40,41]. Moreover, the Z_N of the I_3^-/I^- redox couple in the electrolyte is remarkably reduced when the MWCNT framework is combined with Ni_3S_2, indicating the improvement of electrolyte penetration in CEs [26,42]. Several previous studies have proved that the use of MWCNT composite as a CE material provide some advantages [25–27,40] Firstly, the high surface area and electrical conductivity of MWCNTs not only provides the numerous sites for loading electrocatalytic Ni_3S_2 nanoparticles but also improves the electron transport. Furthermore, the interconnected MWCNT network facilitates the penetration of redox electrolyte. To further investigate the stability of Ni_3S_2/MWCNT-NC CE, the freshly prepared dummy cells and the 20-days aged ones were analyzed by EIS. As shown in Fig. 4b, a slight decrease in R_{ct} value is observed after aging for 20 days, which is possibly attributed to the better contact or the enhanced I_3^- reduction reaction at electrolyte/CE interface. [43] This result signifies that the Ni_3S_2/MWCNT-NC CE is electrochemically stable in the corrosive I_3^-/I^- based electrolyte.

To further prove the results from EIS analyses, Tafel-polarization measurements were carried out. Fig. 5 shows the Tafel-polarization curves of symmetrical cells based on Pt, Ni_3S_2, MWCNT, and Ni_3S_2/MWCNT-NC CEs. Generally, the exchange current density (J_0) can be obtained in the Tafel region, which is determined from the intersection of the cathodic branch and the equilibrium potential line. J_0 values for the individual CEs are summarized in Table 1. In theory, J_0 value inversely depends on the R_{ct} value, as illustrated in Eq. (1) [44].

$$J_0 = \frac{RT}{nFR_{ct}} \tag{1}$$

where R is the gas constant, T is the absolute temperature, F is the Faraday constant, and n is the number of electrons involved in the reaction at the electrolyte/CE interface. Compared with the pristine Ni_3S_2 (0.83 mA cm^{-2}) and MWCNT (0.25 mA cm^{-2}) CEs, the Ni_3S_2/MWCNT-NC CE possesses an enhanced J_0 value (2.66 mA cm^{-2}) and this value is close to that of Pt CE (3.11 mA cm^{-2}). The variance tendency of the R_{ct} value calculated from the J_0 value for the Pt, Ni_3S_2, MWCNT and Ni_3S_2/MWCNT-NC CEs is in accordance with that obtained in the EIS measurements. Moreover, the limiting diffusion zone located at the very high potential zone is associated with the transport of electrolyte, in which the limiting current density (J_{lim}) can be determined from the intersection of the
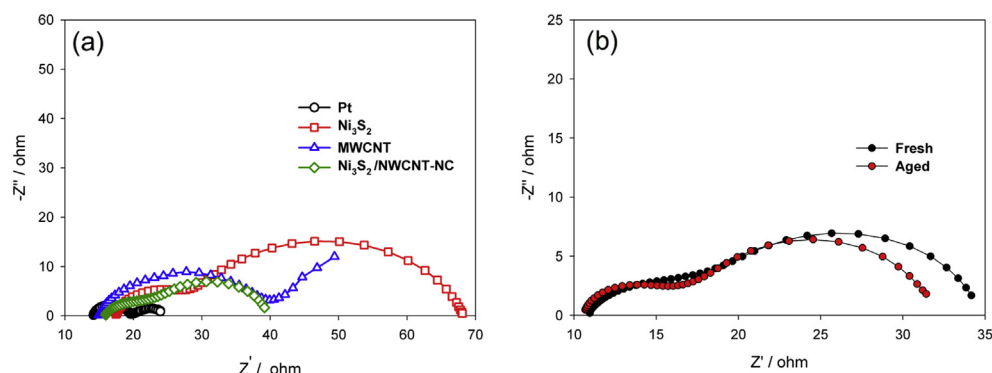
Fig. 4. (a) Nyquist plots of the symmetrical cells assembled with the Pt, Ni_3S_2, MWCNT, and Ni_3S_2/MWCNT-NC CEs. (b) Nyquist plots of the symmetrical cells based on the fresh and 20-day aged Ni_3S_2/MWCNT-NC CEs.
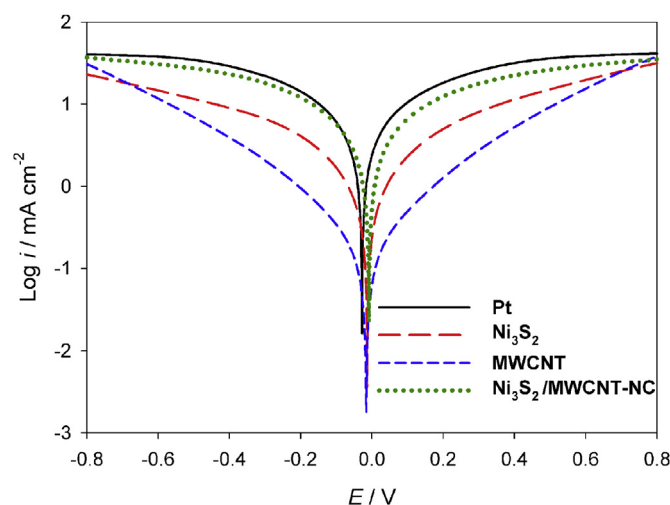
Fig. 5. Tafel polarization curves of the symmetrical cells assembled with the Pt, Ni_3S_2, MWCNT, and Ni_3S_2/MWCNT-NC CEs.

Table 2
Photovoltaic parameters of the DSCs based on the Pt, Ni_3S_2, MWCNT, and Ni_3S_2/MWCNT-NC CEs.

	J_{sc}/mA cm^{-2}	V_{oc}/V	FF	η (%)
Pt	14.16 ± 0.08	0.76 ± 0.01	0.67 ± 0.01	7.24 ± 0.13
Ni_3S_2	12.88 ± 0.31	0.76 ± 0.01	0.58 ± 0.02	5.77 ± 0.07
MWCNT	12.41 ± 0.17	0.72 ± 0.02	0.42 ± 0.02	3.76 ± 0.05
Ni_3S_2/MWCNT-NC	13.96 ± 0.24	0.77 ± 0.01	0.63 ± 0.01	6.87 ± 0.12

cathodic branch with the *y* axis. Basically, J_{lim} is positively related with the diffusion coefficient (*D*) of I_3^- in terms of Eq. (2), in which δ is the spacer thickness, C is the I_3^- concentration, *n* is the number of electrons involved in the I_3^- reduction, and *F* is the Faraday constant. The *D* value illustrates the diffusion character of the I_3^- redox species in the electrolyte [45]. As a result, the diffusion coefficients of the I_3^- species for the pristine Ni_3S_2 and Ni_3S_2/MWCNT-NC CEs were evaluated to be 1.97×10^{-5} and 2.28×10^{-5} cm^2 s^{-1}, respectively. The improved diffusion behavior of I_3^- species in the Ni_3S_2/MWCNT-NC CE may be ascribed to the fact that the introduction of porous MWCNT framework facilitates the electrolyte penetration in CEs, as suggested by the EIS results.

$$J_{lim} = \frac{2nFC}{\delta}D \qquad (2)$$

Fig. 6 shows the photocurrent density−photovoltage curves of the DSCs fabricated with Pt, Ni_3S_2, MWCNT and Ni_3S_2/MWCNT-NC CEs. The corresponding photovoltaic parameters including open-circuit (V_{oc}), short-circuit current (J_{sc}), fill factor (FF), and cell efficiency (η) are also summarized in Table 2. With regarded to the DSC assembled with the MWCNT CE, its η value is only 3.76%. This poor

Fig. 6. Typical photocurrent−photovoltage curves of DSCs assembled with the Pt, Ni_3S_2, MWCNT, and Ni_3S_2/MWCNT-NC CEs, respectively.

η value is mainly attributed to its limited electrocatalytic activity for I_3^- reduction [46]. As for the Ni_3S_2 CE, Ni_3S_2 particles not only are seriously aggregated together but also lack the conductive paths for electron transport in the CE, thus leading to the decrease in the number of electrocatalytic sites and the increase in the resistance for electron transport [40,47]. As expected, the Ni_3S_2 CE based DSC shows the low η value of 5.77% due to the decreased J_{sc} and FF values. Compared with Ni_3S_2 and MWCNT CE based DSCs, the Ni_3S_2/MWCNT-NC CE based DSC shows a higher η value (6.87%) due to the great contribution from the improved FF and J_{sc} values. For the Ni_3S_2/MWCNT-NC based DSC, the increase in J_{sc} value may be attributed to the fact that the large active surface area of CE increases the total current of the I^-/I_3^- redox reaction and therefore facilitates the transport of the generated electrons from photo-anode to CE [19,40,41,48]. Furthermore, the enhancement in the FF value of the Ni_3S_2/MWCNT-NC based DSC can be explained by the decrease in the internal resistance elements (R_s, R_{ct} and Z_N) [49,50]. Due to the superior electrical conductivity of MWCNTs, the Ni_3S_2/MWCNT-NC CE shows a low R_s value, which promotes the collection of electrons from the external circuit. On the other hand, its small R_{ct} due to the synergistic effects of the increased number of electrocatalytic active sites of Ni_3S_2 nanoparticles and the conductive MWCNT framework suggests the enhanced electron transfer from the CE to the I_3^- ions at the CE/electrolyte interface. Furthermore, the low Z_N value for the Ni_3S_2/MWCNT-NC CE implies that the decoration of Ni_3S_2 nanoparticles on the porous MWCNT network can shorten the ionic diffusion path and thus improve the ionic diffusion flux. On the basis of the aforementioned effects, Ni_3S_2/MWCNT-NC CE based DSC shows a comparable photovoltaic performance to the sputtered Pt CE based DSC (η=7.24%). Fig. S5 further displays the long-term stability results for the DSCs based on the Pt and Ni_3S_2/MWCNT-NC CEs, in which the obtained conversion efficiency of the DSCs were recorded in every two days over a period of two weeks. It is found that the DSC based on the Ni_3S_2/MWCNT-NC CE shows comparable conversion efficiency to that using the Pt CE even after two weeks, indicating its reasonable stability in the long-term operation. This result is also consistent with the aforementioned long-term EIS results.

4. Conclusions

We have successfully synthesized Ni_3S_2/MWCNT-NC through a facile hydrothermal method. It is found that the amorphous carbon produced in situ by the hydrothermal carbonization of glucose covers both MWCNT and Ni_3S_2 nanoparticle surface, and therefore serves as a binder to assist the decoration of Ni_3S_2 nanoparticles onto MWCNT surface. We also found the post-annealing treatment is an effective approach to remove the partial amorphous carbon on Ni_3S_2/MWCNT-NC, which increases the active sites of Ni_3S_2 nanoparticles. Compared with the Ni_3S_2 and MWCNT CEs, the Ni_3S_2/MWCNT-NC CE obviously shows an improved electrocatalytic activity. This result is ascribed to the synergetic effects of the fast electron-transfer of the MWCNTs and highly electrocatalytic activity of Ni_3S_2 nanoparticles. Moreover, the Ni_3S_2 nanoparticles highly dispersed on MWCNTs provides more active sites for I_3^-

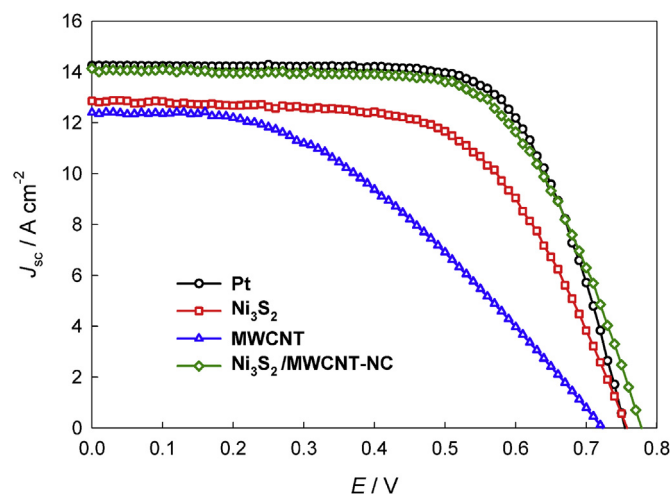reduction and the network of Ni_3S_2/MWCNT-NC facilitates the redox electrolyte diffusion within the CE. Therefore, the DSC assembled with the Ni_3S_2/MWCNT-NC CE exhibits an impressive PCE of 6.87%, which is significantly higher than those of the DSCs based on the Ni_3S_2 CE (5.77%) and MWCNTs CE (3.76%). Because the Ni_3S_2/MWCNT-NC CE based DSC shows a comparable photovoltaic performance to the DSC assembled with the Pt CE (7.24%), Ni_3S_2/MWCNT-NC CE may serve as an inexpensive and promising alternative to Pt CE for DSCs.

Acknowledgments

Appendix A. Supplementary data

Supplementary data related to this article can be found at http://dx.doi.org/10.1016/j.jpowsour.2014.07.041.

References

[1] B. O'regan, M. Grätzel, Nature 353 (1991) 737–739.
[2] H.C. Weerasingle, F. Huang, Y.B. Cheng, Nano Energy 2 (2013) 174–189.
[3] W.J. Lee, E. Ramasamy, D.Y. Lee, Sol. Energy Mater. Sol. Cells 92 (2008) 814–818.
[4] T.N. Murakami, S. Ito, Q. Wang, M.K. Nazeeruddin, T. Bessho, I. Cesar, P. Liska, R. Humphry-Baker, P. Comte, P. Péchy, M.J. Grätzel, J. Electrochem. Soc. 153 (2006) A2255–A2261.
[5] K. Imoto, K. Takahashi, T. Yamaguchi, T. Komura, J.I. Nakamura, K. Murata, Sol. Energy Mater. Sol. Cells 79 (2003) 459–469.
[6] Z. Huang, X. Liu, K. Li, D. Li, Y. Luo, H. Li, W. Song, L.Q. Chen, Q. Meng, Electrochem. Commun. 9 (2007) 596–598.
[7] W.J. Lee, E. Ramasamy, D.Y. Lee, J.S. Song, ACS Appl. Mater. Interfaces 1 (2009) 1145–1149.
[8] P. Brown, K. Takechi, P.V. Kamat, J. Phys. Chem. C 112 (2008) 4776–4782.
[9] J.G. Nam, Y.J. Park, B.S. Kim, J.S. Lee, Scr. Mater. 62 (2010) 148–150.
[10] G. Zhu, L. Pan, T. Lu, X. Liu, T. Lv, T. Xu, Z. Sun, Electrochim. Acta 56 (2011) 10288–10291.
[11] Y. Peng, J. Zhong, K. Wang, B. Xue, Y.B. Cheng, Nano Energy 2 (2013) 235–240.
[12] X. Wang, L. Zhi, K. Mullen, Nano Lett. 8 (2008) 323–327.
[13] A.F. Nogueira, C. Longo, M.A.D. Paoli, Chem. Rev. 248 (2004) 1455–1468.
[14] E. Palomares, J.N. Clifford, S.A. Haque, T. Lutz, J.R. Durrant, J. Am. Chem. Soc. 125 (2003) 475–482.
[15] G.R. Li, J. Song, G.L. Pan, X.P. Gao, Energy Environ. Sci. 4 (2011) 1680–1683.
[16] M. Wu, X. Lin, Y. Wang, L. Wang, W. Guo, D. Qi, X. Peng, X. Hagfeldt, M. Grätzel, T. Ma, J. Am. Chem. Soc. 134 (2012) 3419–3428.
[17] M. Wu, X. Lin, A. Hagfeldt, T. Ma, Angew. Chem. Int. Ed. 50 (2011) 3520–3524.
[18] A. Kaniyoor, S. Ramaprabhu, Nano Energy 1 (2012) 757–763.
[19] J.Y. Lin, J.H. Liao, S.W. Chou, Electrochim. Acta 56 (2011) 8818–8826.
[20] M. Wu, Y. Wang, X. Lin, N. Yu, L. Wang, L. Wang, A. Hagfeldtc, T. Ma, Phys. Chem. Chem. Phys. 13 (2011) 19298–19301.
[21] S.A. Patil, P.Y. Kalode, R.S. Mane, D.V. Shinde, A. Doyoung, C. Keumnam, M.M. Sung, S.B. Ambade, S.H. Han, Dalton Trans. (2014), http://dx.doi.org/10.1039/C3DT53356E.
[22] H. Bi, W. Zhao, S. Sun, H. Cui, T. Lin, F. Huang, X. Xie, M. Jiang, Carbon 61 (2013) 116–123.
[23] H.Y. Wang, F.M. Wang, Y.Y. Wang, C.C. Wan, B.J. Hwang, R. Santhanam, J. Rick, J. Phys. Chem. C 115 (2011) 8439–8446.
[24] E. Ramasamy, W.J. Lee, D.Y. Lee, J.S. Song, Electrochem. Commun. 10 (2008) 1087–1089.
[25] G.R. Li, F. Wang, J. Song, F.Y. Xiong, X.P. Gao, Electrochim. Acta 65 (2012) 216–220.
[26] J. Song, G.R. Li, F.Y. Xiong, X.P. Gao, J. Mater. Chem. 22 (2012) 20580–20585.
[27] J.Y. Lin, J.H. Liao, T.Y. Hung, Electrochem. Commun. 13 (2011) 977–980.
[28] L. Zhang, H.K. Mulmudi, S.K. Batabyal, Y.M. Lam, S.G. Mhaisalkar, Phys. Chem. Chem. Phys. 14 (2012) 9906–9911.
[29] Y. Xiao, J. Wu, J.Y. Lin, G. Yue, J. Lin, M. Huang, Y. Huang, Z. Lan, L. Fan, J. Mater. Chem. A 1 (2013) 13885–13889.
[30] Y. Yan, X. Ge, Z. Liu, J.Y. Wang, J.M. Lee, X. Wang, Nanoscale 5 (2013) 7768–7771.
[31] H. Wang, J.T. Robinson, G. Diankov, H. Dai, J. Am. Chem. Soc. 132 (2010) 3270–3271.
[32] C.S. Dai, P.Y. Chien, J.Y. Lin, S.W. Chou, W.K. Wu, P.H. Li, K.Y. Wu, T.W. Lin, ACS Appl. Mater. Interfaces 5 (2013) 12168–12174.
[33] S. Ding, J.S. Chen, X.W. Lou, Chem. Eur. J. 17 (2011) 13142–13145.
[34] T.W. Lin, C.J. Liu, C.S. Dai, Appl. Catal. B (2014), http://dx.doi.org/10.1016/j.apcatb.2014.02.017.
[35] Q. Li, J. Wu, Q. Tang, Z. Lan, P. Li, J. Lin, L. Fan, Electrochem. Commun. 10 (2008) 1299–1302.
[36] J.Y. Lin, C.Y. Chan, S.W. Chou, Chem. Commun. 49 (2013) 1440–1442.
[37] Z. Lan, J. Wu, J. Lin, M. Huang, J. Mater. Chem. 22 (2012) 3948–3954.
[38] J.Y. Lin, S.Y. Tai, S.W. Chou, J. Phys. Chem. C 118 (2014) 823–830.
[39] S. Gagliardi, L. Giorgi, R. Giorgi, N. Lisi, T.D. Makris, E. Salernitano, A. Rufoloni, Superlattices Microstruct. 46 (2009) 205–208.
[40] S.Y. Tai, C.J. Liu, S.W. Chou, F.S.S. Chien, J.Y. Lin, T.W. Lin, J. Mater. Chem. 22 (2012) 24753–24759.
[41] Z. Li, F. Gong, G. Zhou, Z.S. Wang, J. Phys. Chem. C 117 (2013) 6561–6566.
[42] Q.W. Jiang, G.R. Li, F. Wang, X.P. Gao, Electrochem. Commun. 12 (2010) 924–927.
[43] C. Bu, Y. Liu, Z. Yu, S. You, N. Huang, L. Liang, X.Z. Zhao, ACS Appl. Mater. Interfaces 5 (2013) 7432–7438.
[44] A.J. Bard, L.R. Faulkner, Electrochemical Methods: Fundamentals and Applications, second ed., John Wiley & Sons, New York, 2001, p. 115.
[45] M.K. Wang, A.M. Anghel, B. Marsan, N.C. Ha, N. Pootrakulchote, S.M. Zakeeruddin, M.J. Grätzel, J. Am. Chem. Soc. 131 (2009) 15976–15977.
[46] A. Kongkanand, R.M. Dominguez, P.V. Kamat, Nano Lett. 7 (2007) 676–680.
[47] F. Gong, X. Xu, Z. Li, G. Zhou, Z.X. Wang, Chem. Commun. 49 (2013) 1437–1439.
[48] J.Y. Lin, W.Y. Wang, Y.T. Lin, S.W. Chou, ACS Appl. Mater. Interfaces 6 (2014) 3357–3364.
[49] L. Han, N. Koide, Y. Chiba, A. Islam, R. Komiya, N. Fuke, A. Fukui, R. Yamanaka, Appl. Phys. Lett. 86 (2005) 213501.
[50] F. Malara, M. Manca, L.D. Marco, P. Pareo, G. Gigli, ACS Appl. Mater. Interfaces 3 (2011) 3625–3632.